Viorel Ilinca · Ionuț Șandric · Zenaida Chițu · Radu Irimia · Ion Gheuca

UAV applications to assess short-term dynamics of slow-moving landslides under dense forest cover

Abstract The paper presents a methodology to rapidly assess and map the landslide kinematics in areas with dense vegetation cover. The method uses aerial imagery collected with UAVs (Unmanned Aerial Vehicles) and their derived products obtained from the structure from motion technique. The landslide analysed in the current paper occurred in the spring of 2021 and is located in Livadea village from Curvature Subcarpathians, Romania. This landslide affected the houses in the vicinity, and people were relocated because of the risk of landslide reactivation. To mitigate the landslide consequences, a preliminary investigation based on UAV imagery and geological-geomorphological field surveys was carried out to map the active parts of the landslide and establish evacuation measures. Three UAV flights were performed between 6 May and 10 June using DJI Phantom 4 and Phantom 4 RTK UAVs (Real-Time Kinematic Unmanned Aerial Vehicles). Because it is a densely forested area, semi-automated analyses of the landslide kinematics and change detection analysis were not possible. Instead, the landslide displacement rates and the changes in terrain morphology were assessed by manually interpolating the landmarks, mostly tilted trees, collected from all three UAV flights. The results showed an average displacement of approximately 20 m across the landslides, with maximum values reaching 45 m in the transport area and minimum values below 1 m in the toe area. This approach proved quick and efficient for rapid landslide investigations in a densely forested area when fast response and measures are necessary to reduce the landslide consequences.

Keywords Landslide mapping · UAV · Kinematics · Multitemporal · Trees · Cracks

Introduction

Since the beginning of the landslide research, methods and guidelines for landslide mapping and assessment were developed to integrate highly cost-effective technologies. Among them, InSAR (Carnec et al. 1996; Delacourt et al. 2007; Fustos et al. 2017; Schulz et al. 2017; Tarchi et al. 2003), optical (Delacourt et al. 2007; Dille et al. 2021; Manconi et al. 2014; Türk 2018) or GPS (Benoit et al. 2015; Gili et al. 2000; Li et al. 2017; Squarzoni et al. 2005) has been widely used to map and assess the landslide kinematics and surface deformations. More recent, applications of LiDAR from both aerial and terrestrial perspectives have been used to map and monitor the landslide kinematics (Alberti et al. 2020; Booth et al. 2020, 2018; Conforti et al. 2021; Pellicani et al. 2019; Schulz 2007; Van Den Eeckhaut et al. 2007). Both InSAR and LiDAR are expensive technologies and require either high-resolution SAR imagery or expensive field campaigns when detailed studies are requested.

Recently, with the development and advancement of the technology, new tools, like consumer-grade UAVs, were introduced for landslide mapping. These new technologies are more appropriate, faster and more accurate than the traditional ones (Booth et al. 2020). In recent years, many studies used aerial images collected with UAV equipped with RGB cameras to map and/or to assess in detail the landslide kinematics of at least one landslide (James et al. 2017; Lucieer et al. 2014; Niethammer et al. 2012; Rossi et al. 2018; Stumpf et al. 2013). Many of these studies used lightweight UAVs, usually with payloads less than 2 kg. According to Giordan et al. (2018), Gomez and Purdie (2016) and Kucharczyk and Hugenholtz (2021), the UAVs have broad applications in geosciences, starting from the generation of very detailed 2D and 3D products (like orthophotos, digital surface models, etc.) and moving towards detection in quasi-real-time.

The most used technique for processing imagery collected with UAVs is structure from motion (SfM), an image-based method that uses many images taken from various locations and at different angles to determine the position of a particular object (Carey et al. 2019; Rossi et al. 2018; Valkaniotis et al. 2018). Unlike classic photogrammetry, in the case of SfM, the images can be acquired randomly, not necessarily in forward and side stripes. SfM uses an algorithm for image matching, such as scale invariant feature transform or SIFT (Lowe 2004, 1999) computer vision algorithm, that detects and match local features from images. According to Fonstad et al. (2013), SfM may give results similar to those obtained employing Lidar and can be used widely given the much lower costs (Fonstad et al. 2013; Westoby et al. 2012) in comparison with LiDAR. Although the images may be randomly taken, in the case of geoscience applications, it is highly recommended to collect them in a regular grid with forwarding and side overlaps of at least 70% and from a constant height above the terrain (Cheng et al. 2021; Lindner et al. 2016; Rossi et al. 2018).

UAVs are suitable for emergencies, geo-hazard monitoring, landform mapping and monitoring physical processes or estimation of landslide kinematics. The use of the UAV is present in the pre-event, during the event and in the post-event phases, but in the case of applications to landslides, most of the studies, to our knowledge, were focused so far on post-events. A considerable number of studies presented rapid assessments of landslides kinematics and the damages caused by those. Such approaches were described for rapid assessment of rockfall (Giordan et al. 2015; Santangelo et al. 2019) or by using multitemporal flights (Lindner et al. 2016; Lucieer et al. 2014; Peternel et al. 2017; Rossi et al. 2018; Yang et al. 2021; Zárate et al. 2021). Multitemporal flights were also used to estimate the landslide kinematics and detect changes in the terrain's

morphology by implying techniques such as DEMs of difference (DoD) (Brasington et al. 2000; Wheaton 2008; Williams 2012). The DoD approach assumes that the data obtained from UAVs have a very high spatial accuracy so that the uncertainty is as low as possible and can be estimated (Wheaton et al. 2010). Another approach is the estimation of the landslide kinematics by mapping the deformations induced by the sliding process across the terrain surface (Fleming et al. 1999). These deformations of the landslide surface usually follow a pattern that includes stretching, shortening, shearing, tilting and rotation (Baum and Fleming 1991) depending on landslide type. In this case, analysis of the landslide kinematics is based on the mapping of landslide features (Baum and Fleming 1991; Fleming et al. 1999; Fleming and Johnson 1989; Guzzi and Parise 1992; Schulz et al. 2017). The amount of displacement rate and landslide kinematics computed from successive aerial imagery using different points such as trees or rocks were reported by Baum and Fleming (1991). Fleming et al. (1999) used fracture patterns, split trees and stretched roots to assess the landslide kinematics. Other approaches in assessing the landslide kinematics are using the UAV images to map landmarks located on the body of landslides from multiple flights. A displacement rate can be computed by calculating the distances between identical landmarks for different periods. This approach works better in forested areas than DoD, where the digital surface and elevation models are negatively influenced by the presence of vegetation and the limitations of RGB cameras.

The current study focuses on using UAV imagery and their derived products, like orthophotos, digital surface and elevation models, for rapid mapping and assessing the dynamics of slow-moving landslides under forested areas. Two consumer and enterprise-grade UAVs, DJI Phantom 4 and Phantom 4 RTK, were used to collect the aerial imagery at a constant height above the ground. Instead of using an automated evaluation method of the landslide kinematics, a semi-automated one was preferred based on manually collected points across the entire landslide (space and time). The reasons for choosing a manual mapping of key landslide kinematics

points are related to the high level of uncertainties present in areas with dense vegetation cover, and these elevation uncertainties can have a significant propagation in subsequent landslide analyses (Huang et al. 2021; Qin et al. 2013; Sandric et al. 2019). Landmarks, such as tilted trees, fissures and fractures, were used to estimate the landslide kinematics for all the flights between 6 May and 10 July 2021. The reason for doing so is related to the high elevation uncertainties present in areas with dense vegetation cover, where the automated calculus of the differences between two digital elevation/surface models is prone to significant errors caused by the canopy height and vegetation cover changes. The displacement rates were calculated based on the points collected between two consecutive flights. A map with the spatial distribution of the displacements was obtained from the interpolation of these points.

Materials and methods

Study area

The Livadea landslide is located within the Vărbilău watershed, Teleajen Subcarpathians (Fig. 1a, b), a subdivision of the Curvature Subcarpathians. It is a hilly area with gentle to moderate slopes and elevation ranging between 260 and 770 m. The general orientation of the main rivers is from north to south, and rounded ridges delimit their watersheds. The Telejean Subcarpathians are areas with high activity and density of landslides, controlled mainly by the local geological setting (Popescu-Voiteşti 1924; Vîrghileanu 2018).

Geology and geomorphologic settings

From a tectonic point of view, the area overlaps the Tarcău Nappe (Fig. 2a), in close contact with the post-tectonic units with Lower Miocene tectogenesis (Ştefănescu et al. 1978). The oldest formation is the *Plopu Formation* (Eocene), formed from clayey-sandy flysch with intercalation of red clay and marls (Fig. 2b, c). In the
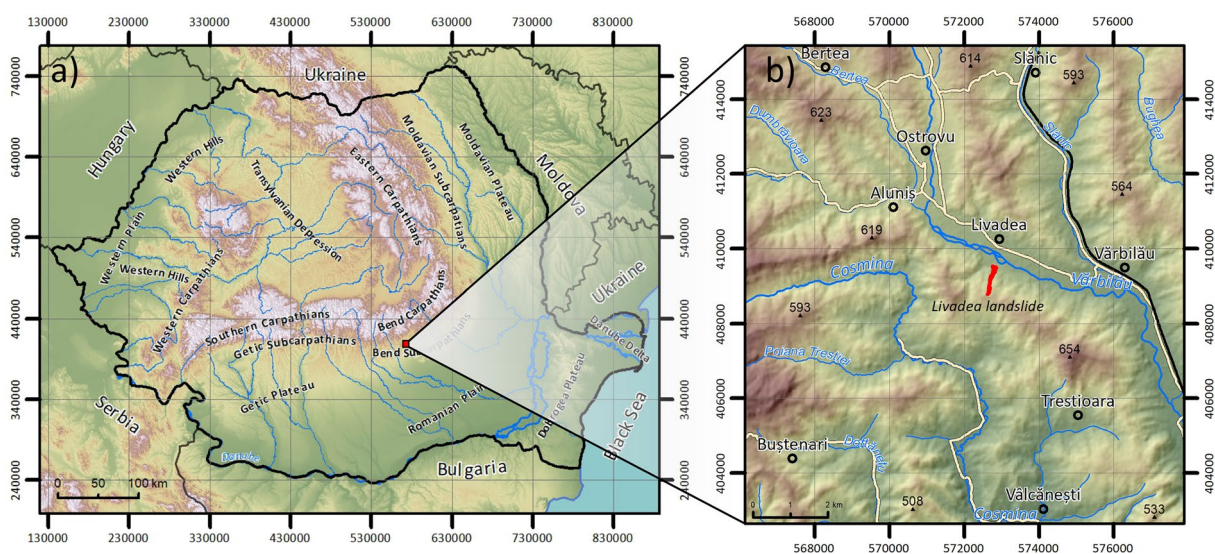

Fig. 1 Location of Livadea landslide within: (**a**) Romania and (**b**) Vărbilău watershed (DEM based on SRTM90 (Farr et al. 2007))
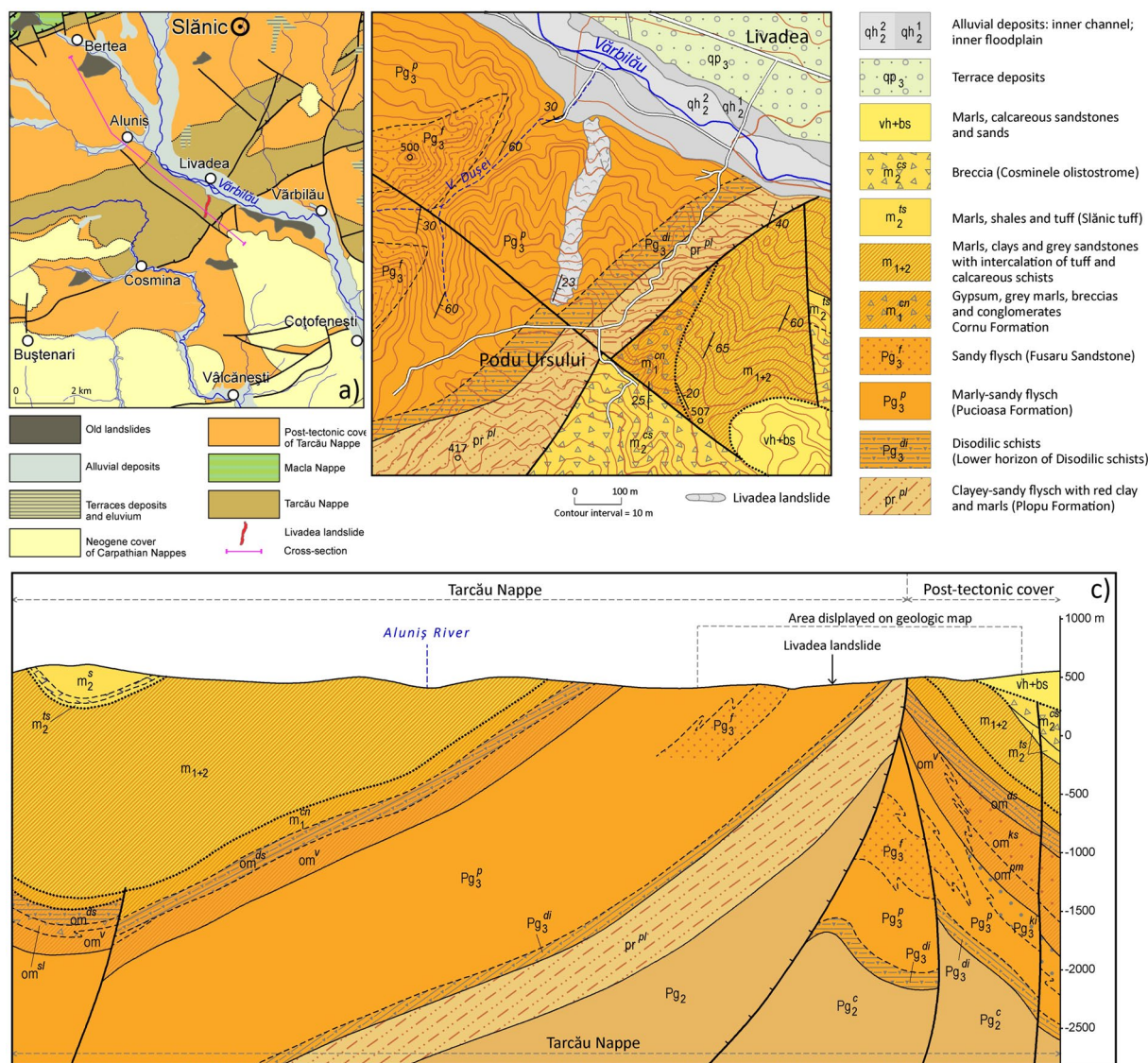
Fig. 2 (**a**) Tectonic map of Livadea area (compiled and simplified from Ștefănescu et al. 1978 and Pătruț 1955); (**b**) geologic map of the Livadea area (Ștefănescu et al. 1978) with minor modifications; (**c**) geologic cross-section (Ștefănescu et al. 1978). Symbols that appear on the cross section and that are not presented on the maps: Pg2c, Colți Formation (Eocene); Pg3ki, Lower Kliwa sandstone (Oligocene); ompm, Podu Morii Formation (Oligo-Miocene); omv, Vinețișu Formation (Oligo-Miocene); omsl, Slon Formation (Oligo-Miocene); omds, the lower horizon of disodilic schists (Oligo-Miocene); m2s, Salt Formation (Middle Miocene)

stratigraphic succession, the subsequent units are the *Lower horizon of Disodilic schists Formation* (Oligocene), formed mostly from disodilic schist. The next formation is the *Pucioasa Formation* (Oligocene), which consists of marly-sandy flysch, and it is the layer in which the Livadea landslide occurred. Also, during the Oligocene, a sandier formation was deposited over the Pucioasa Formation named *Fusaru Formation*. The contact between the Eocene rocks of the Tarcău Nappe and its sedimentary cover occurs along a reverse fault with the SW-NE strike. To the east of this reverse fault, newer deposits appear with heterogeneous lithology and ages between the Lower Miocene and Middle Sarmatian (Popescu 1952; Ștefănescu et al. 1978).

The geological formations presented above are covered by superficial deposits such as soil and regolith, as seen in the landslide scarp (see Fig. 9a). It consists of fine materials such as silt and clay. A relatively large volume of these deposits was entrained in the landslide mass. The map presented in Fig. 2a was slightly adjusted using the high-resolution aerial imagery and the field observations. The modifications of the map consist of the following: the adjustment of the Quaternary deposit limits (gh1, qh2 and qp3); of the geologic limit between Pg3p and Pg3di based on the new outcrops provided by the landslide scarp; one structural measurement point (dip/dip angle) located on the landslide scarp was added; the latest landslide body was drawn

over the original geological map; and other map elements, like hydrography, roads and peaks were added as layers in the original map.

Landslide occurrence

The Livadea landslide was triggered on 3 May 2021, at approximately 19:00 h. The triggering time was associated with the noises made by a large volume of rock and colluvium detached from the headscarp. According to the local inhabitants, the sliding process was slow, with speeds of a few meters per day, and it continued until the morning of 7 May 2021. In the initial stage, the landslide lobe destroyed one house and its household annexes and stopped at about 1 m from another house. The household annexes from the second house were also affected. During the night between 7 and 8 May 2021, a reactivation of the landslide created a second lobe located on the western part of the main accumulation area (primarily lobe). Both landslide lobes barely reached the Vărbilău floodplain, stopping a few meters after the contact between the plain and the hilly area. The third reactivation of the landslide occurred on 6 July 2021, when the eastern lobe (the initial lobe) moved a few meters towards the Vărbilău River and destroyed the second house. A third lobe appeared eastward of the main lobe of the landslide.

The current landslide occurred in an area with evident landforms (old hummocks) left from past landslides as well as many tilted trees. As seen in Fig. 3a, the landslide moved downslope on a small pre-existent valley (channelised landslide) which also imprinted the sliding direction.

At the sliding time, almost the entire area was forested (Fig. 3b).

Hydro-meteorological characteristics

The precipitation regime in this area is mainly influenced by the moisture of air masses coming from the Mediterranean basin and less by those coming from Western Europe (Antofie 2007). The mean annual precipitation, calculated for the period 1985–2015 at the Câmpina weather station, is 741.6 mm, reaching a maximum value in June (106.6 mm) and a minimum value (32.2 mm) in February (National Administration of Meteorology n.d.). The mean annual temperature is 9.4 °C, with the highest values during July (20.4 °C) and lowest values in January (−1.1 °C) (National Administration of Meteorology n.d.). The regional hydrologic regime of the study area reflects both the meteorological conditions and the geologic characteristics of the drainage area. The presence of flysch deposits in this specific area determines a low soil infiltration capacity and a flashy character of the stream. These characteristics are highlighted by the low values of the baseflow index (0.40) and the recession rate (0.85) and by the high value (6250 (l/s/km²) of the peak discharge (Chitu et al. 2017). The value of the peak discharge is calculated for a recurrence interval of 100 years (Q 1%) and using data recorded at Vârbilău-gauging station (National Institute of Hydrology and Water Management n.d.).

The investigation of the regional hydro-meteorological conditions recorded previously of the Livadea landslide occurrence revealed a significant increase in the volume of water stored in the Vârbilău catchment from January to April 2021. During the last 4 months before the landslide occurrence, the study area received
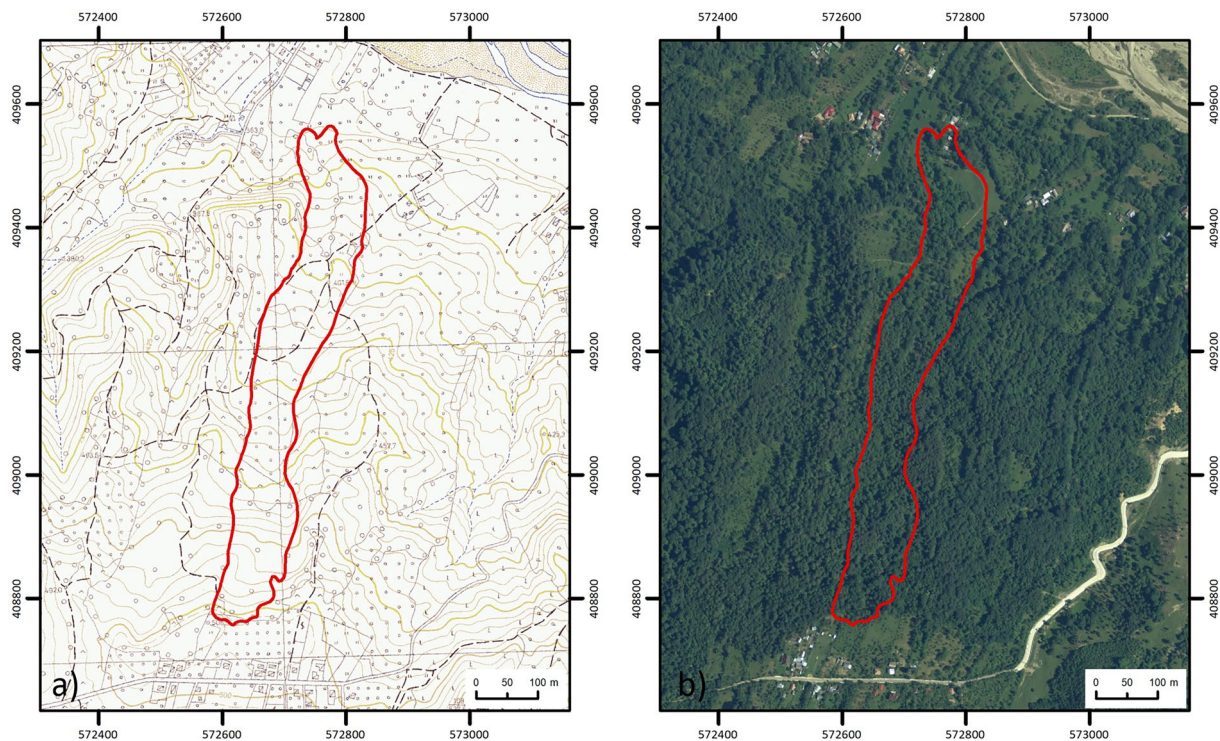

Fig. 3 Livadea landslide (red line) draped on (**a**) topographic map at scale 1:5.000 (ANCPI 1965) and (**b**) orthophoto from 2016 (ANCPI). Note that the landslide area was forested at the time of the landslide occurrence
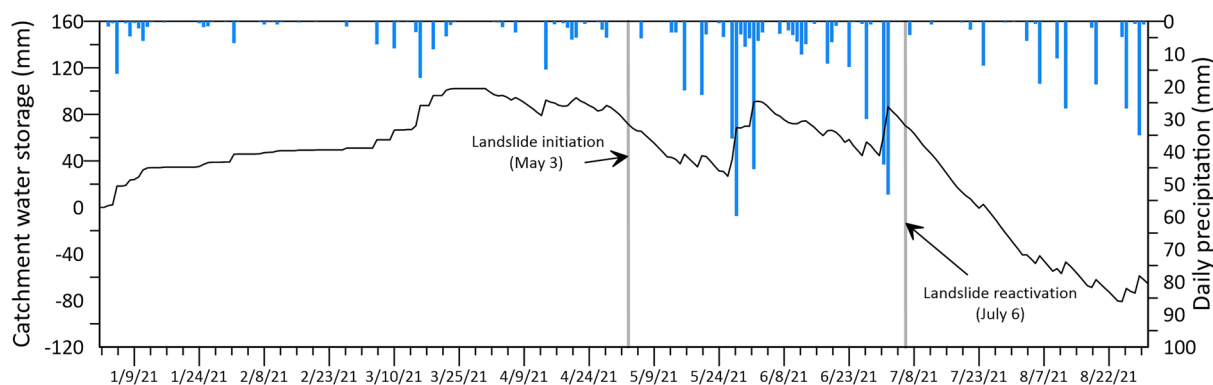
Fig. 4 Hydro-meteorological conditions between 1 January and 31 August, 2021, Vârbilău catchment

a near-normal amount of precipitation. The alternation of snow-melt and low-intensity precipitation from the cold period produced favourable conditions for soil water infiltration. In addition, the lack of evapotranspiration and soil evaporation generated a high catchment water storage. All these conditions explained the first slope failure that occurred on 3 May 2021 (Fig. 4) and made it possible to move down a huge volume of earth. Immediately after this event, numerous springs were visible along the hillslope, showing that the soil was completely saturated with water. During the next three months (May–July), the study area received more than 450 mm precipitation, but only one reactivation was recorded on 6 July 2021. These high intensities and short duration convective rainfalls produced peak discharges on the main hydrological stream.

The occurrence of the Livadea landslide confirmed the slow accumulation of water into the soil during the cold season when snowmelt is overlapped on low-intensity rainfalls and low evapotranspiration/soil evaporation, producing the most favourable conditions for landslide initiation in shale deposits and surficial deposits from above.

Data acquisition and methods

Most of the dataset used to assess the Livadea landslide kinematics was obtained by applying image interpretation techniques on aerial imagery collected with UAVs. Additional information about the landslide predisposing and triggering factors was obtained from old orthophotos and satellite imagery, detailed topographical maps, geological maps, field surveys and local inhabitants (affected or not by the landslide).

Conceptual model workflow

The workflow used in the current paper (Fig. 5) is based on UAV imagery collection and processing with the structure from motion (SfM) technique to produce high spatial resolution orthophotos, digital surface and elevation models. The structure from motion is a method from computer vision that uses multiple stereo images, which have a side and forward overlap of at least 70%, to reconstruct the 3D surface of the objects. It has been around since 1976 (Ullman 1983, 1976), and it was used sporadically in the 1980s (Bolles et al. 1987; Fischler and Bolles 1981). With the recent acceleration in computing performance and the

development of more reliable UAVs, the use of SfM has known a drastic increase in the last 15 years in various scientific domains
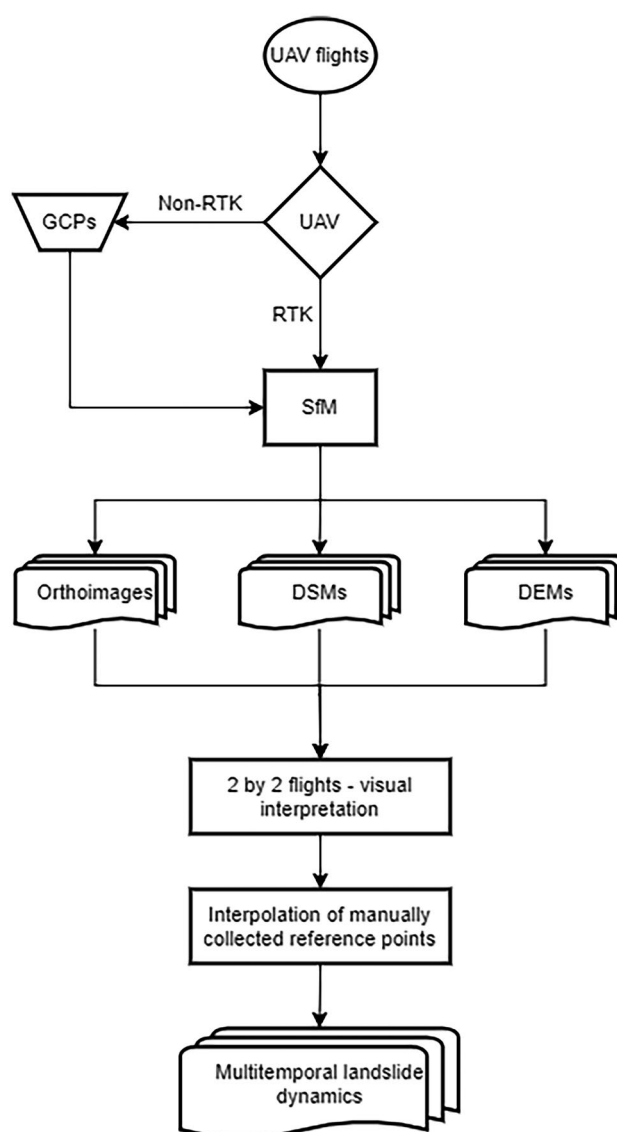

Fig. 5 Flow chart of the conceptual model used to assess the kinematics of the Livadea landslide

and study of landslides too (Fonstad et al. 2013; Rossi et al. 2018; Ullman 1979; Valkaniotis et al. 2018; Westoby et al. 2012; Zárate et al. 2021). The main products obtained from the SfM process are point clouds with the X, Y, Z and RGB spectrum information attached to each point. Derived products such as digital surface models, ortho imagery and digital elevation models are obtained from the cloud point data.

Based on the products obtained from the SfM process, manually collected reference points are interpolated to generate a continuous surface with the landslide displacement rates between two-time intervals. By combing the results obtained from the two by two analyses, the final multitemporal landslide kinematics was obtained.

UAV flights

The first UAV flight was performed three days from the initial occurrence of the landslide, on 6 May 2021. For this flight, a DJI Phantom 4 quadcopter with a 12-MP RGB camera was used, through which 1115 images were collected. Because the exact location of the landslide was not known, the first flight plan was constructed to cover a wider area than the actual landslide location. The following flights were planned on the orthophoto obtained from the first flight. Thus, fewer images were necessary to cover the entire area of the landslide. The next two flights were performed on 25 May and 10 July 2021 using a DJI Phantom 4 RTK UAV with a 20-MP RGB camera. Even though there is a difference in camera resolution, each flight plan was created to correspond to approximately 4 cm/pixel spatial resolution, meaning that the constant height above the ground was different between the first flight and the next two flights (Table 1). All the flights were planned and executed using the Universal Ground Control System software (UGCS) produced by SPH Engineering.

Only the second and third flights were performed with a UAV equipped with an RTK receiver from all three flights. For the first flight, because the UAV equipped with the RTK receiver was not available, a graded consumer UAV equipped with a non-RTK receiver was used. To ensure an optimal overlap with the smallest possible errors, the first flight was orthorectified using the Ground Control Points (GCPs) collected from the second flight, flown with a UAV equipped with an RTK receiver. Even though it was flown with a UAV equipped with an RTK receiver, the third flight had many images collected without RTK because of the high radar interference from the study area. Similar to the first flight, the third flight was also orthorectified using GCPs collected from the second flight.

Image processing

All the flights were processed using ArcGIS Drone2Map software (ESRI n.d.) that is using the SfM engine provided by Pix4D company ("Professional photogrammetry and drone mapping software | Pix4D") (PIX4D SA C n.d.). The following products were obtained for each flight using the ArcGIS Drone2Map: an orthophoto map, a digital elevation model (DEM) and a digital surface model (DSM). The products obtained from the second flight (25 May 2021) were used as a base reference for reprocessing the other two flights: 6 May and 10 May 2021. Ground control points were collected on top of the orthophoto and DSM from the second flight (for each point, the longitude, latitude and elevation were extracted) and further used in the reprocessing of the UAV flights from 6 May and 10 June 2021. By applying this technique, we ensured an optimal overlap between the products of the all three flights, with an RMS values below 10 cm on X and Y and below 70 cm on Z (Table 2). One reason for reprocessing the third flight is related to the high radio interference in the area of the Livadea landslide, which affected more than 60% of the images collected with the RTK receiver. For the SfM process of the first and the third flight, a number of six points were used. More points were not possible to collect because of the high canopy cover on the landslide body. The overlap of the products obtained from each flight was validated using 19 points distributed evenly across the entire landslide. The RMS values for both GCPs (SfM processing and validation) are presented in the table below.

Field surveys

During the landslide occurrence and movement, several field surveys were conducted in spring 2021 (6th, 23th and 25th of May). A detailed geomorphological map containing all the landslide features was produced and validated during these field surveys.

Table 1 UAV flights information

Flight date	UAV	Pixel resolution (m)	Height above ground (m)	Side and forward overlap	Images captured (no.)	Area (ha)
6 May 2021	DJI Phantom 4	0.035	81	70%	1115	94
25 May 2021	DJI Phantom 4 RTK	0.035	117	70%	456	75
10 July 2021	DJI Phantom 4 RTK	0.035	117	70%	455	75

Table 2 Properties of the orthophoto, DSM and DEM derived from UAV aerial imagery

Flight date	Orthophoto resolution (m)	DSM resolution (m)	DEM resolution (m)	RMS (GCPs) (m)	RMS (validation GCPs) (m)
6 May 2021	0.03	0.03	0.16	*X*: 0.025968 *Y*: 0.015673 *Z*: 0.025248	*X*: 0.168017 *Y*: 0.134719 *Z*: 0.468118
25 May 2021	0.03	0.03	0.16	*X*: 0.014693 *Y*: 0.020548 *Z*: 0.055997	*X*: 0.080317 *Y*: 0.067928 *Z*: 0.584534
10 June 2021	0.03	0.03	0.16	*X*: 0.043112 *Y*: 0.050032 *Z*: 0.075169	*X*: 0.103392 *Y*: 0.080315 *Z*: 0.690356

Some structural measurements were made below the headscarp of the landslide, where a few outcrops are present. A similar detailed investigation was done in the middle and lower part of the landslides, where minor scarps are located, and an echelon fractures system takes place. All the field surveys were performed using a smartphone equipped with a GPS receiver. The accuracy of points collected in the field for mapping the landslide features was about 1.5 m, and the location of these features was further adjusted based on aerial imagery acquired with the UAVs.

Landslide feature mapping

A combination of orthophotos and terrain parameters like hillshade, slope, and curvature (Wilson and Gallant 2000) was used as the primary dataset to interpret the landslide morphology visually. Based on these datasets, the landslide features, such as the crown, headscarp, shear planes, fractures, fissures, tilted trees, roads, damaged houses and adjacent buildings, were mapped in very great detail. The process of visual interpretation of aerial images was done in a GIS environment using ArcGIS Pro 2.8 (ESRI). All the landslide features were mapped on the orthophotos and aerial imagery and were further verified, validated and corrected during the field campaigns. Landslide features as slickensides or hidden cracks in the forest have been identified during the field investigation and added to the map. A detailed geomorphological map containing all the landslide features mapped on the field or by image interpretation has been drawn at a scale of 1:2500. Special cartographic symbols, created and used as True Type Fonts within the ArcGIS Pro 2.8 (ESRI n.d.) based on symbols described in the literature (Baum and Fleming 1991; Fleming et al. 1999; Fleming and Johnson 1989; Guzzi and Parise 1992; Parise 2003) and Federal Geographic Data Committee (FGDC) guideline (USGS 2006), were used, modified and adjusted. The original map was initially drawn at a scale of 1:1.000 and was reduced to a scale of 1:2.500 for publication purposes.

Displacement rate assessment

Because there is a high density of trees on the landslide surface, automated detection of the landslide kinematics is challenging to achieve. To overcome this issue, landmarks, such as trees trunks or fractures patterns, were used to calculate the displacement rates

between two successive flights (Baum and Fleming 1991; Fleming et al. 1999; Fleming and Johnson 1989; Guzzi and Parise 1992; Schulz et al. 2017). Thus, it was possible to calculate displacement rates for two-time intervals: from 6th May to 25th May and 25th May to 10th July. Even with this technique, there were areas on the landslides where it was impossible to estimate a displacement rate using landmarks. These areas correspond to translational movements where the trees remained vertical, despite the high displacement rate. For these cases and to have a homogeneous distribution of the displacements across the entire landslide, it was preferred to collect as many as possible displacement points manually and to interpolate them using the Inverse Distance Weighted (IDW) interpolation method. The IDW was preferred due to its robustness in using the non-normal distribution of the displacements rates. An iteration over the IDW interpolation parameters was conducted, and the best parameters reported by the cross-validation process were selected.

Results

Landslide morphology

Based on the data collected in the field and the products obtained from the aerial imagery processing, the landslide was spatially delineated with very high accuracy (less than 10 pixels errors, where one pixel has 3 cm spatial resolution). The general direction of the landslide is from south-southwest to north-northeast, except for the depletion zone where the landslide direction is changed towards the north (Fig. 6a–c). The headscarp of the landslide is visible on all the orthophotos, given that it is in high contrast with the surrounding forested area. Its crown is located at 510 m elevation, while its toe is at an elevation of 360 m, with an elevation range of 150 m. The landslide length is 850 m (calculated as the major axis of the boundary polygon), while the height to length ratio (*H/L*) is 0.18, meaning that the overall slope of the landslide is a moderate one. The landslide area increased from 7.78 ha on the 6th of May to 7.9 ha on the 25th of May and reached 8.49 ha on the 10th of June. During the field study, the height between the crown and the basal shear plane of the landslide was measured. Based on these measurements, the average landslide depth was estimated at approximately 5 m, making the total volume of the landslide about 424.500 m³. Conversely, based on the crown height and the basal slickenside of the landslide headscarp (detached area), it was estimated that the slip surface occurred at a depth of approximately 10 m.

Fig. 6 Landslide spatial distribution mapped on orthophotos obtained by drone flights: (**a**) 6 May; (**b**) 25 May; (**c**) 10 July 2021
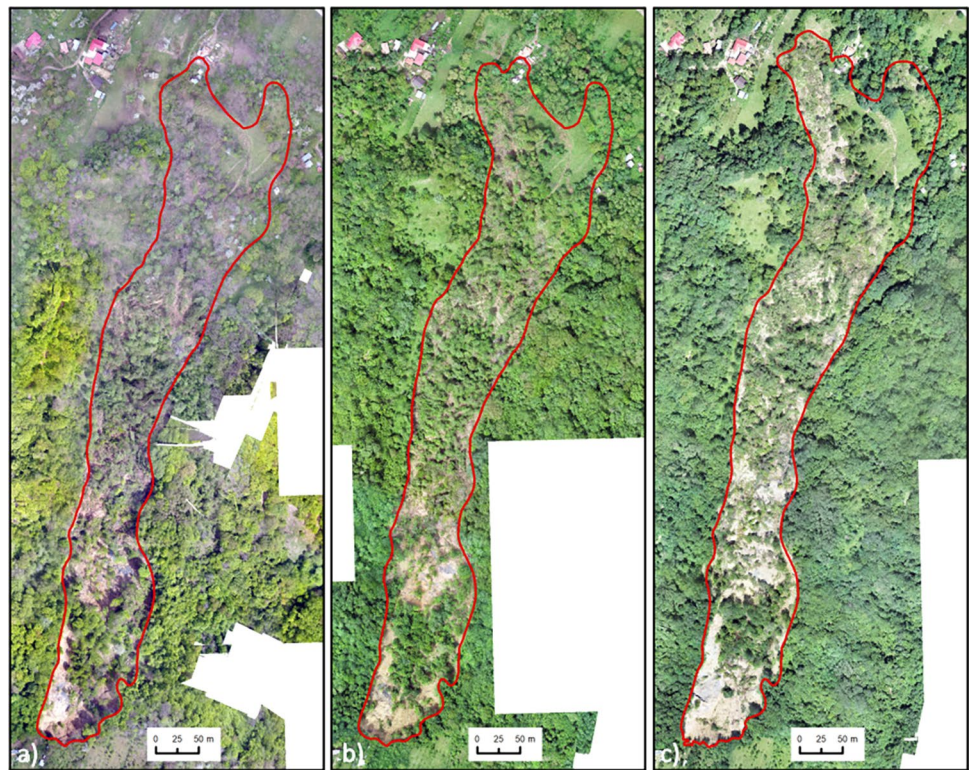
The landslide morphology (Figs. 7 and 8) is quite complex. Besides the headscarp, several secondary scarps are distributed along with the longitudinal profile, with areas of stretching and shortening and the presence of slickensides.

The headscarp (Fig. 9a–d) has a typical arched shape having a height of about 10 m and a maximum width of about 90 m. The field surveys revealed that it was developed in a sequence of sedimentary rocks, mostly composed of layered grey marls with thin intercalations (subcentimetric) of disodilic schist. Almost the entire headscarp is covered by soil and colluvium, with the bedrock appearing only in a few outcrops. The field measurements in two of the outcrops located on the landslide scarp showed that the bedding dips to 110° (east-southeast) with values between 15 and 23°, while the detachment area slides to 20° (north). Therefore, the detachment occurred on an orthoclinal slope (the slide is perpendicular to the bedding). This is specific to the Curvature Subcarpathians, where, among lithology, the landslide occurrences are strongly related to the geological structure (Ilinca et al. 2021).

A large quantity of the material was detached from the headscarp and transported to approximately 160 m downslope, forming

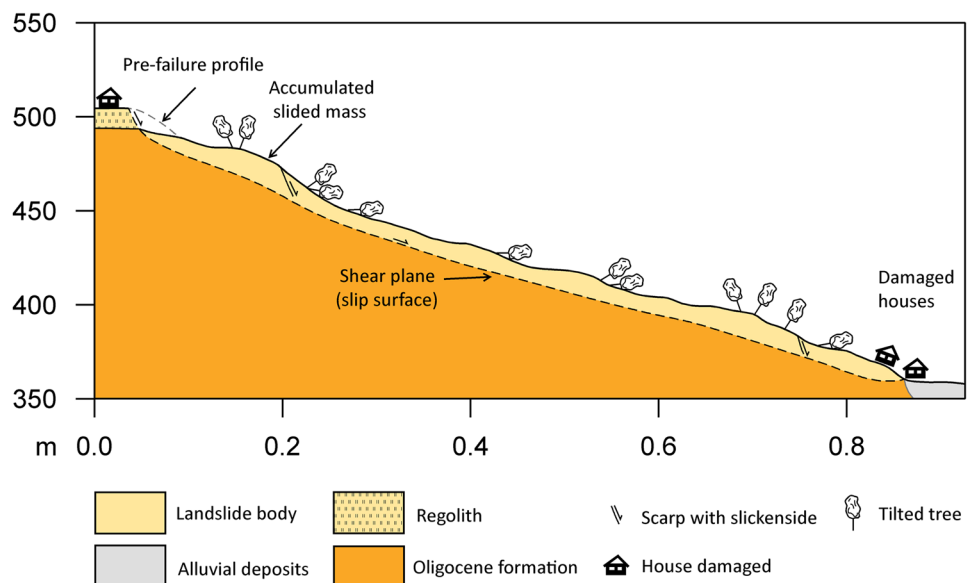**Fig. 7** Synthetic geologic cross-section through Livadea landslide

Fig. 8 Detailed map of the landslide: (**a**) headscarp and a section from the transport area; (**b**) a section from the transport area and the depletion area. The landslide map was drawn based on the aerial imagery from the first flight and field survey from 25th of May. Only the lobes formed later were displayed here, although the map represents the early stage of the landslide
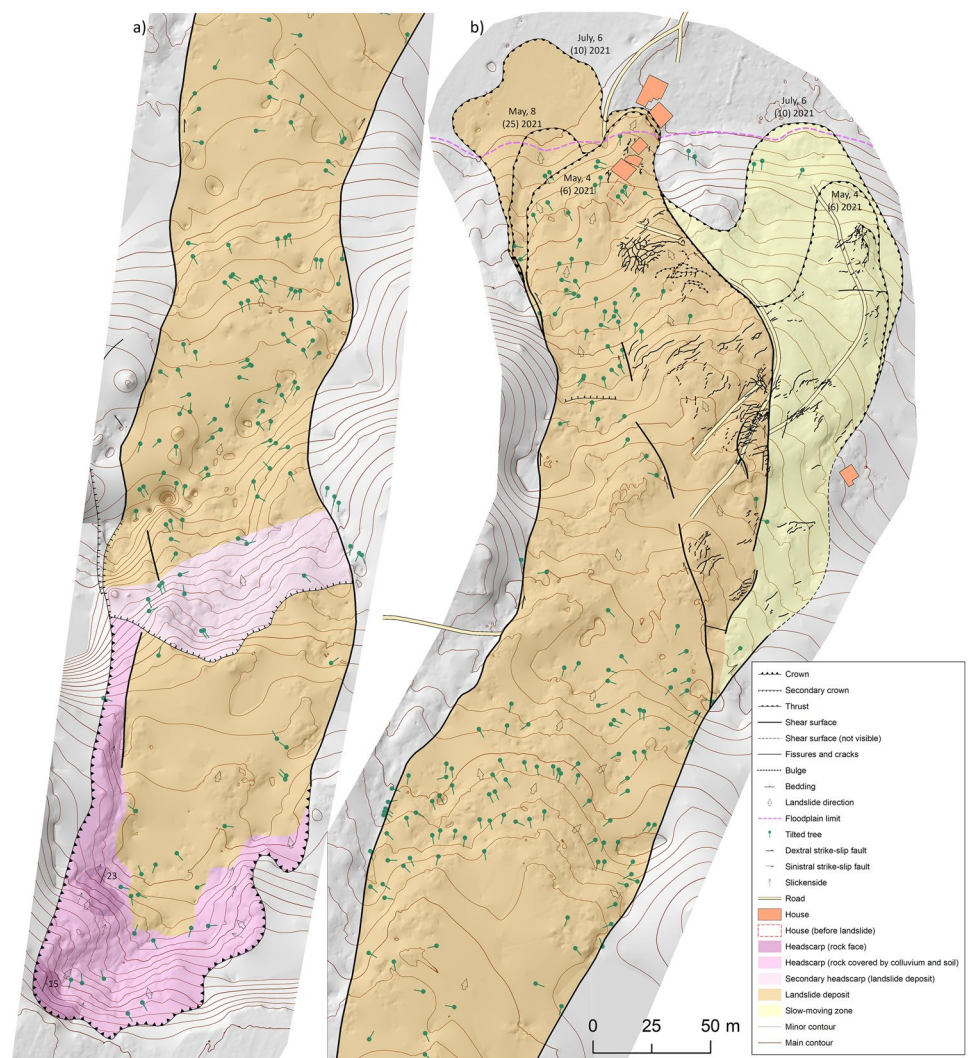
a relatively flat area. Here, the landslide deposits probably have the largest thickness estimated to be about 20 m. Based on the aspect of the headscarp, the orientation of many slickensides, the direction of the tilted trees and the detachment of the rock and colluvium took place along a planar slip surface which indicates a translational mechanism. This assertion is strictly valid only for the detachment area because the landslide swifts into a clear translational slide towards downslope.

The transport area starts at approximately 474 m elevations, has about 535 m in length and is 70–110 m wide. The flanks of the landslide are bounded by the shear plane (left-lateral shear in left flank and right-lateral shear in right flank) (Fig. 10a–d). Whereas in the upper sector of the transport zone, the landslide is bounded by a 2–5-m lateral scarp, sometimes with cracks behind it, in the lower sector, the shear plane is exposed. In some cases, the shear plane is concealed by recent deposits (soil and colluvium) that are detached from lateral minor scars or deposits of the landslide itself. Overall, the landslide body is bounded by flank ridges ranging from 2 to 3 m. In the lower part of the transport zone, multiple shear surfaces occur toward the right flank (F2, F3 and F4). On the right shear plane (F3), many fissures and fractures occur in an echelon system. An important secondary scarp

is located at 170 m downslope from the main crown, having 20 m in height. From this point forward, the material is continuously eroded.

The boundary between the transport and depletion zones is unclear, so the limit between them was traced arbitrarily. In the depletion zone, two lobes occurred at a short period between them (Fig. 11). The first lobe (L1), oriented from south-southwest to north-northeast, merely reached the floodplain, destroyed a house and some household annexes and stopped at a one-meter distance from the second house (Fig. 12a, b). The second lobe (L2) is located on the east side of the L1 lobe. The third lobe (L3) was formed west of the L1 and had a slightly different direction oriented more towards the north. Later, between 5 and 6 July 2021, all lobes (L1–L3) advanced further toward the floodplain. The central lobe (L1) reached the second house (Fig. 12c), which had to be dismantled and rebuilt in the vicinity. The L2 advanced 30 m, while the L3 advanced even further with almost 40 m. In the case of L3, the first displacement was observed shortly (8th of May) after the landslide was triggered and remained stable at least until 25th of May, when the second flight was conducted. During the reactivation from the beginning of July, L3 advanced in two distinct directions and formed two sublobes: L3a and L3b.

Fig. 9 Headscarp characteristics: (**a**) overview of the headscarp; (**b**) outcrop with grey marls and thin intercalation of disodilic schists; (**c**) fracture in the basal shear plane (grey marls); lateral landslide (soil and colluvium with trees) feeding the main landslide. The red arrows indicate the landslide direction
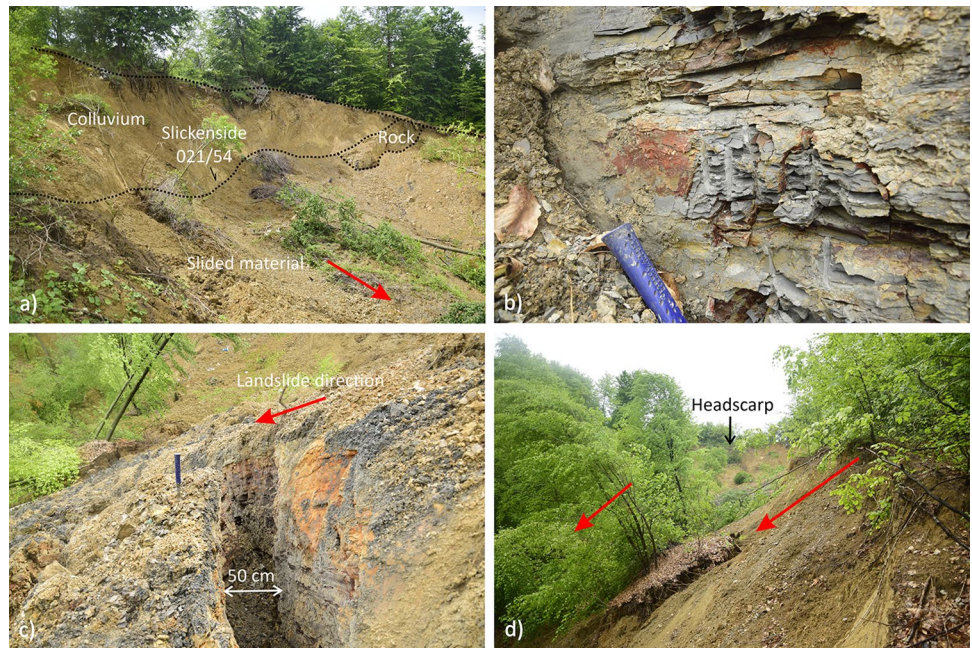
Most of the landslide flanks are bounded by strike-slip faults, except the upper zone where a U-shaped crown is present. The left flank of the landslide is visible, except for some areas where the lateral shear-plane (sinistral strike-slip fault) is concealed by deposits that were detached from the nearby small scarps. The right flank is delimited by a visible shear plane (dextral strike-slip fault), and in the lower part, strike-slip faults occur. In the lower part of the landslide, other dextral strike-slip fault systems cross the landslide body with a SE-NW strike. Many echelon fractures (Fig. 13a) occur along the right flank at an angle that usually ranges between 20° and nearly perpendicular, being a typical shear zone in these types of landslides. Other features such as bulges, thrust along lateral strike-slip flank and lobes were also identified and mapped within this zone (Fig. 13b–d). Herein, while the landslide direction is generally from south to north (Figs. 14a and 15a), the cracks and fractures are oriented obliquely (Figs. 14b and 15b).

Fig. 10 Left flank with slickenside (**a**, **b**); right flank with share plane (**c**, **d**). The red arrow indicates de landslide direction

Fig. 11 The landslide toe in different periods. The coloured line represents the location and extension of each lobe as mapped on the UAV aerial images. The dates with black arrows indicate the exact date of the event based on information obtained from the local inhabitants. The background image is from 10 July 2021 flight
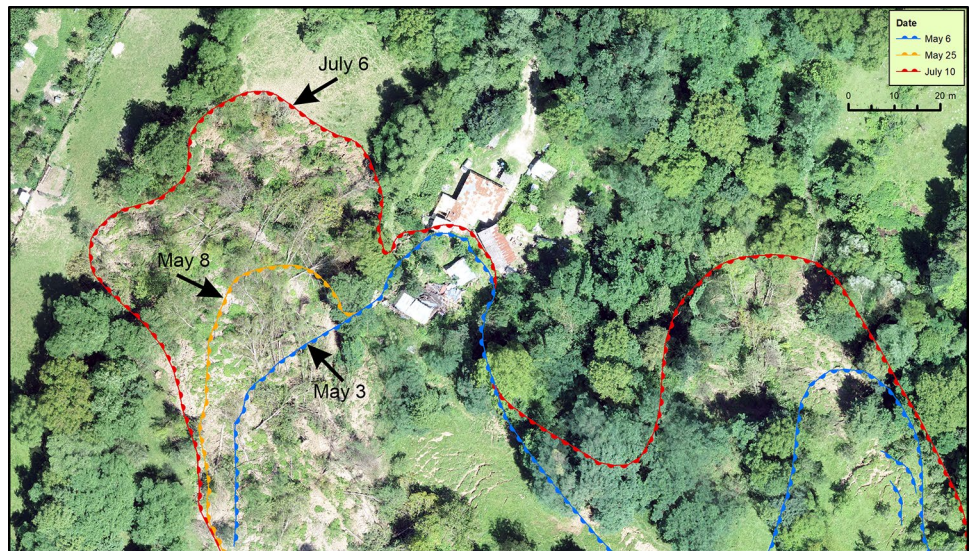

Fig. 12 The landslide toe: (**a**) view to upslope and (**b**) view to downslope (photo taken on 25 May 2021); (**c**) the landslide toe reached the house on 6 July 2021 (photo credit: Daniel Ioniță). The red arrow indicates the same corner of the house

Fig. 13 Landslide features from the depletion area: (**a**) echelon fractures along the shear plane; (**b**) buckle fold or bulge; (**c**) right-lateral share plane that tends to overthrust the adjacent area (shear surface dip with 77° into the landslide body); (**d**) the eastern lobe of the landslide that thrust old landslide deposits. The red arrows indicate the landslide direction
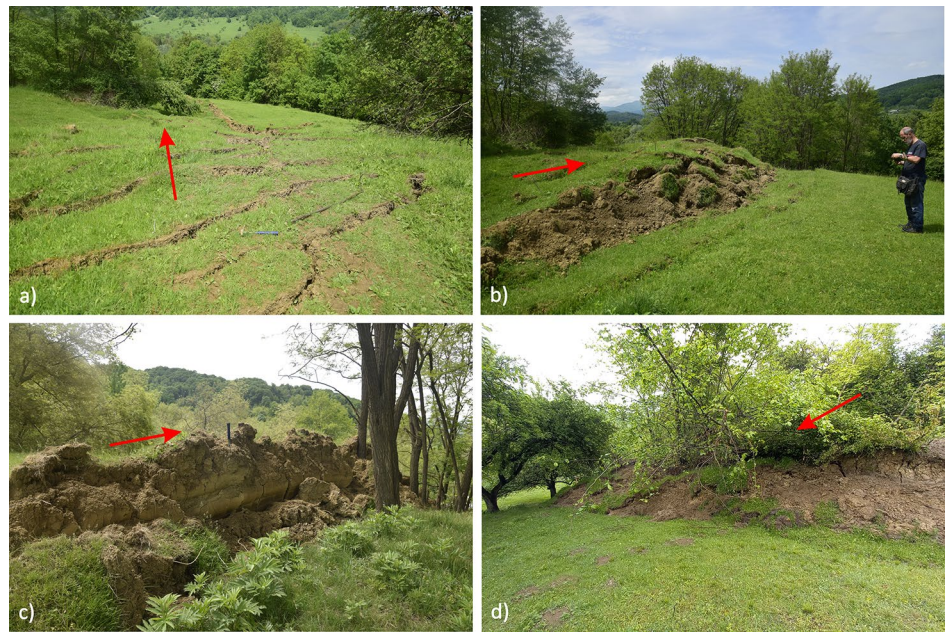
Fig. 14 A shear zone on the right flank of the landslide: (**a**) aerial images were taken on 6th of May; (**b**) extracted faults and fissures. Note the strike-slip fault (right-lateral — thick black line) and associated cracks and fissures (thin black line). Note that many fissures are oriented obliquely to the shear plane (displacement of about 15 m)
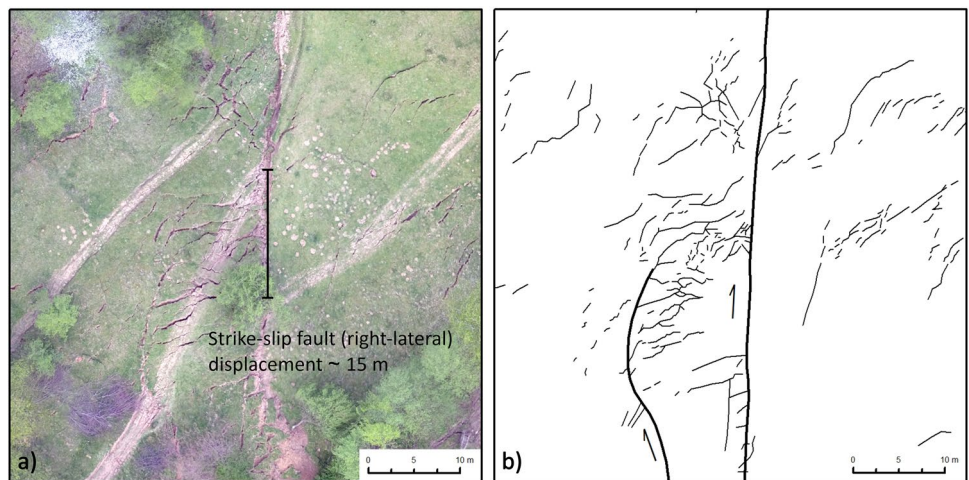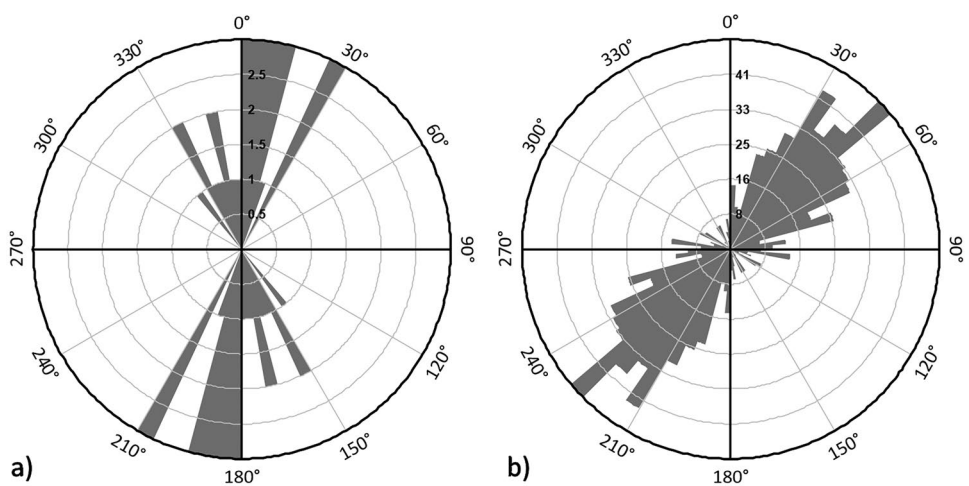
Strike-slip fault (right-lateral) displacement ~ 15 m

Fig. 15 Rose plot for (**a**) shear planes (*n* = 22) and (**b**) fissures and cracks (*n* = 528)

Landslide kinematics assessment from UAV aerial imagery and SfM products

Because at the time when the landslide was triggered, the area was completely forested, it was not possible to correctly evaluate the topography of the landslides, so the displaced trees and other landmarks were used to understand and map the direction and amplitude of the landslide mass. From the UAV aerial imagery, it was possible to see that most of the trees are tilted forward (Fig. 16a–d), which indicated that the landside has a translational mechanism. Only a few trees located on the landslide body are tilted backwards, suggesting a rotational detachment mechanism, but overall, the evidence shows that the mechanism was translational. The trees tilted to the west and east (quasi-perpendicular to the main landslide direction) are a result of the shear in the strike-slip fault zone. Some trees are tilted outward from the landslide, and others are twisted. In some sectors, tilted trees' directions and patterns indicate landslide material overflow in the adjacent zone. In the middle of the

landslide (Fig. 16c), it can be seen from the tilted trees that an internal lobe is radially dissipated. This aspect is evident also from the landslide morphology.

Topography changes between the UAV flights

6 May to 25 May 2021   Between 6 and 25 May 2021, the biggest part of the landslide remained relatively stable, with a few exceptions located in the landslide toe. A maximum displacement rate of 20.6 m was found in the landslide toe, located in the area between F1 and F2 (Fig. 17a, b). This area was the most active, with average displacement values estimated between 18 and 20 m. The material located on the stretching area at 55 to 110 m upslope from the toe was pushed on the floodplain and formed a new lobe (L3) located west of the first one (L1). Other detected movements are indicated by very small displacement rates, of 1 to 2.2 m, located downslope from the minor scarps. The regressive erosion in the headscarp recorded between these two flights has fed the landslide with

Fig. 16 (**a**) The map presents the direction in which the trees are tilted in respect to the landslide direction (the inset presents a rose diagram generated from 300 tilted trees); (**b**)–(**d**) tilted trees as seen from orthophotos
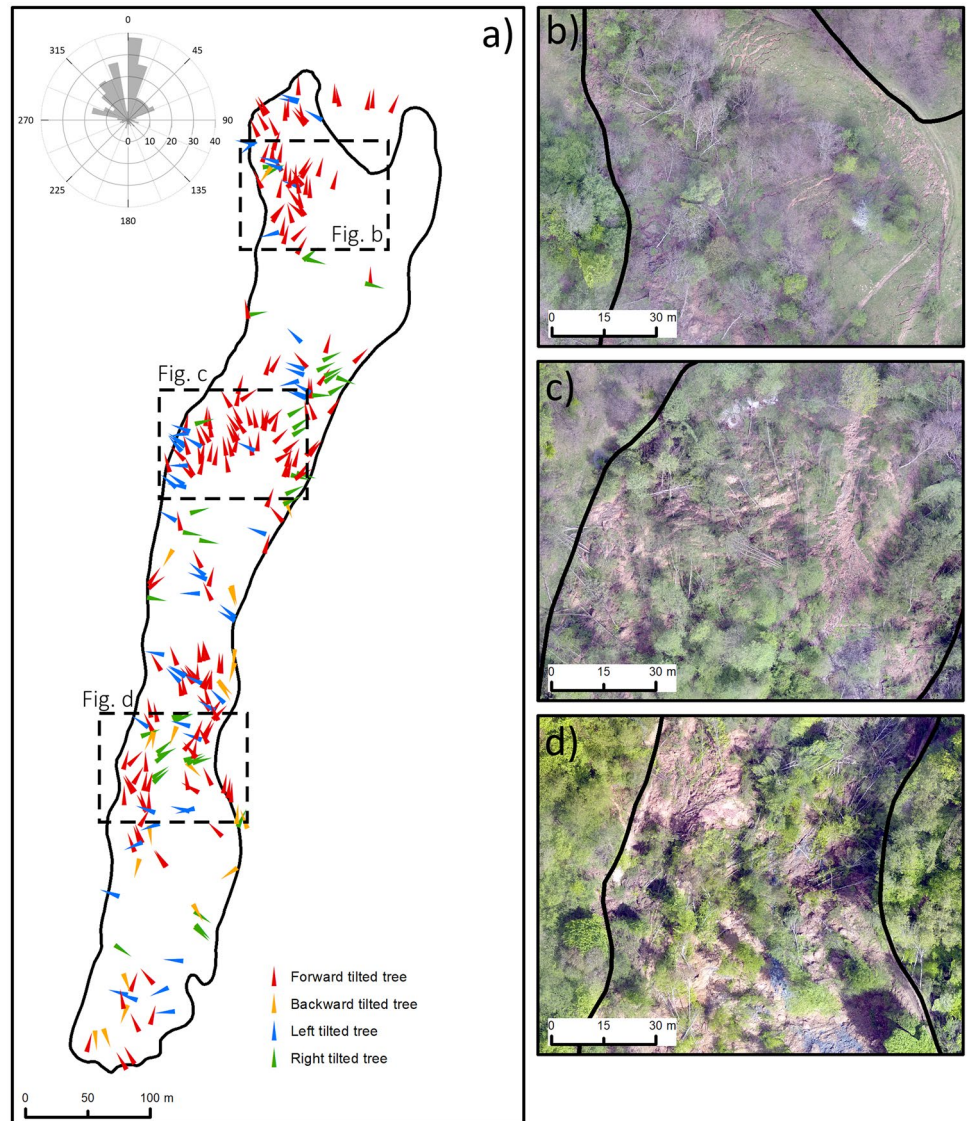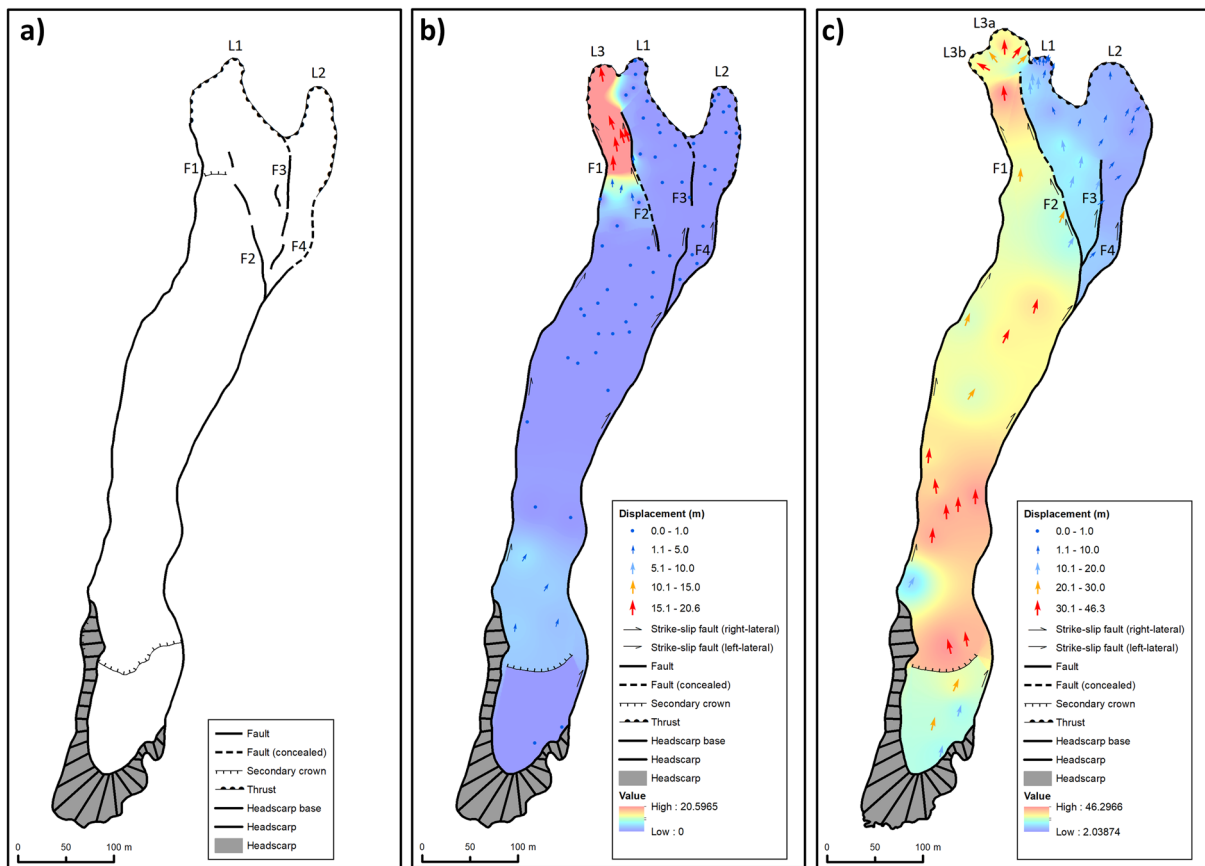
Fig. 17 Map of the landslide displacement rates in meters: (**a**) 5th May — base reference; (**b**) displacement rates between 6th May and 25th May; (**c**) displacement rates between 25th May and 10th July. The displacement points were interpolated using IDW

additional material and many trees. Between the flights, the second lobe (L2) remained mostly stable, although centimetric displacement is very likely to have taken place.

25 May to 10 July 2021   Between 25th May and 10th July, the topography of the landslide has undergone significant changes (Fig. 17c), and most of the landslide has been reactivated. Differences were observed all over the landslide, starting from the headscarp and moving towards the transport and depletion zones. The crown retreated upslope with 7 to 8 m, which implied detachment of additional material, mostly rock, debris, weathered material and many more trees.

A maximum displacement of 46.3 m was measured in the upper part of the landslide, close to the secondary scarp. The average displacement rates are between 21 and 45 m and are mostly located in the middle part of the landslide and the depletion zone.

The displacement rates were very different between the shear surfaces on the depletion zone. Based on that, the depletion could be separated as follows: F1–F2 area (with high displacement rate) and F2–F4 area (with low displacement rate).

The higher displacement rate is in the area of the landslide located between the F1 and F2 faults, which led to the detachment of the larger volume of material and trees, further advancing the

landslides towards the Vărbilău floodplain. The newly accumulated material formed the third lobe (L3), spread radially and composed from two distinct smaller lobes (L3a and L3b; Fig. 17c).

The lower displacement rates were recorded east of the F2 fault, in the area between the F2 and F4 faults. Here, the sliding process was translational, with trees that remained standing. Bounded by the two dextral faults, F2 and F4, the sector was moved approximately 4–15 m to the north and northwest. Inside this sector, two subsectors can be distinguished with different displacement rates, higher to the west and lower to the east, separated by the third fault (F3). The displacement rates are from 10 to 15 m in the area delimited by the F2 and F3 faults (first subsector) and 4 to 7 m in the area delimited by the F3 and F4 faults (the second subsector).

Towards the eastern flank, delimited by a strike-slip faults system (F2 to F4 on Fig. 17c), the sliding process had lower displacement rates than the western flank. The areas located to the east of the F2 fault slipped very little (less than 1 m) or remained stable across all the flights.

Considering all of the above information, including those collected during the field study, the areas located between F1 and F2 faults were considered earthflow (debris and rock fragments are in a negligible proportion), and the area between F2 and F4 faults was considered an earthslide.

Discussions

The current paper provides an inside into rapid mapping of large landslides, triggered in areas with dense vegetation cover and using consumer/enterprise-grade UAVs equipped with RGB cameras. Even though the work has been performed only on one landslide, the results presented in the current paper have sufficient information for further applications of the current methodology (Lindner et al. 2016; Rossi et al. 2018).

UAV flights

During the flights from 6 May to 10 June, a total number of 2026 images have been collected and processed. Each flight was individually processed using ArcGIS Drone2Map software (ESRI), and RMS values below 10 cm have been obtained for each of the three flights. This accuracy is valid for six GCPs used in the SfM processing steps. The RMS values obtained for the GCPs used to verify the quality of the final products (19 points) were a bit higher, still below 1 m, ranging from about 6 cm to about 70 cm. The RMS values below 10 cm are valid for X and Y directions, and RMS values from 46 to 69 cm are valid for Z direction. The values, in line with similar studies (Lindner et al. 2016; Rossi et al. 2018), were achieved by using precise flight plans created with Universal Ground Control System flight planning software (SPH Engineering n.d.) and a constant height above ground, calculated for a 4-cm pixel spatial resolution. The number of GCPs used in processing the flights from 6 to 10 May 2021 is six (Lindner et al. 2016), considered enough to have constant accuracy across the study area. It was impossible to use a higher number of GCP because of the high density of trees located on the landslide body that negatively influenced the accuracy of the GCPs collected in those areas. Overall, the RMS values obtained for all the flights were below 1 m. Hence, in the analysis step, to eliminate all the possible errors induced by the accuracies of the SfM process, only displacements higher than 1 m on X, Y and Z directions were used.

The average processing time was about 1.5 h for all the steps (image matching, point cloud extraction, orthophoto, DSM and DEM extractions) using a laptop equipped with an AMD Ryzen 7 4800H CPU, 16 GB of RAM and an NVIDIA RTX 2060 with 6 GB of RAM. An extra 30 min was added for placing the GCPs on the aerial imagery, being in line with other similar works (Rossi et al. 2018). The processing time is expected to decrease, as the performance of the computers is expected to rise in the near future.

Landslide morphology — fissures and fractures

By applying image interpretation and fusion techniques between the orthophotos and the DSM-derived products (hillshade, slope and curvature), the mapping of fissures and fractures was possible even for the smallest ones, with widths below 10 cm, very similar to values reported by other studies (Samia et al. 2017; Yang et al. 2021). The identification and mapping of the shear zones that accompanied the landslide were also possible using the fissures and fractures mapped from the aerial imagery. Based on the displacement rates and the field surveys, it was concluded that the right lateral part of the landslide toe is a very slow-moving earthslide (F2–F4 zone). This is specific to reduced deformations because almost all the trees stand up without almost any tilting. The higher displacement rates from other areas, like the left side of the landslide toe, are explained by a higher accumulation of water and a partial transformation of the landslide into a flow type (earthflow). The earthflow has a more chaotic morphology, with higher displacement rates determined by the amount of water and trees tilted mainly forward. Instead, the morphology from the earthslide sectors is more straightforward, with faults, fractures and fissures well preserved and with most of the trees in a vertical position. Thus, the lower displacement rates recorded within the earthslide sectors made the trees to move slowly downslope without tilting or uprooting.

All the landslide features mapped from image interpretation were validated during the fieldwork from 25th May when the second flight was flown. More than 90% of the mapped landslides features were validated. The issues related to false positives landslide features were primarily found in areas with long and dark shadows caused by the high and dense vegetation.

Landslide kinematics

Because of the high density of trees located on the landslide surface, an automated and semi-automated process for calculating the landslide kinematics across space and time (Devoto et al. 2020; Niethammer et al. 2012; Rossi et al. 2018) was not possible to fully implement for the current case study. Instead, by interpolating the manually collected reference points, visible between at least two consecutive flights, it was possible to have a constant estimate of the landslide kinematics across the entire landslide. In those areas with high vegetation cover, the uncertainties for the landslide kinematics would have been much higher than areas with low vegetation cover, hence an uneven distribution of the landslide kinematics across the landslide. The highest displacement rate was calculated in the transport area, and it was recorded for the period between the second and the third flight. The lowest displacement rate was calculated for the eastern part of the toe area, with values below 5 m. However, the small number of measurements made in areas challenging to interpret because of the lack of targets can explain the alternation of the displacement rates. However, it is certain is that the landslide movement close to the toe was made in two main directions and delimited by two shear planes.

As previously discussed, the vegetation cover poses the most significant difficulties in mapping the landslide kinematics. To better discriminate between vegetated and non-vegetated areas, future works should focus on using multispectral camera sensors or on the use of UAVs equipped with LiDAR sensors. The availability of LiDAR sensors mounted on UAVs has been increasing in the last couple of years, and it is expected to become very affordable in the near future. It is estimated that the combination of multispectral cameras with LiDAR sensors can bring essential advantages for precise mapping of the landslide kinematics in areas located under dense forests.

In the current study, a detailed field survey has replaced the absence of multispectral and LiDAR cameras, reaching very encouraging results, close to those expected by using more expensive equipment. The difference is that the LiDAR can highlight (detect)

certain features of the landslide hidden by trees that only need to be checked in the field, while UAV products cannot detect such features under the forest. Thus, they must be mapped directly in the field, leading to increased time and costs allocated for the field survey.

Conclusions

With the increasing availability of UAV technology, a considerable number of studies have used consumer and enterprise-grade UAVs for mapping and analysis of recent landslides. In the case of the Livadea landslide, rapid mapping was possible using DJI Phantom 4 Non-RTK and RTK UAVs. The mapping made possible the identification and classification of the landslide as being translational type started as an earthslide and partially evolved into earthflow in the toe area (F1–F2 zone).

Using manually collected GCPs to estimate the landslide displacement rate made it possible to overcome the problems generated by the high density of trees located on the landslide surface. The use of tilted trees mapped as reference points across the entire landslide from UAV imagery made it possible to detect and track the landslide displacement. The direction in which the trees were tilted provided the necessary information to classify the landslide as being mainly translationally. Different displacement rates across space and time were able to calculate, as it is in the depletion area for the Livadea landslide.

The field study offered important information that was a substitute for the absence of multispectral and LiDAR cameras. In combination with the field measurements, the multitemporal UAV surveys led to an optimal understanding of the mechanism and dynamics of the landslide mass in a relatively short time. In less than 1 day after each UAV flight, it was possible to estimate the landslide displacement rates across the entire landslide surface.

Overall, the use of UAV has proven an excellent tool in rapid mapping and analysis of slow-moving landslides in areas with a dense vegetation cover.

Funding

Declarations

Competing interests The authors declare no competing interests.

References

Alberti S, Senogles A, Kingen K, Booth A, Castro P, DeKoekkoek J, Glover-Cutter K, Mohney C, Olsen M, Leshchinsky B (2020) The Hooskanaden Landslide: historic and recent surge behavior of an active earthflow on the Oregon Coast. Landslides 17:2589–2602. https://doi.org/10.1007/s10346-020-01466-8

ANCPI (1965) Topographic plan 1:5000, sheet L-35-100-B-d-3-IV (Podul Ursului). Agenția Națională de Cadastru și Publicitate Imobiliară, Bucharest

Antofie T (2007) Studiu climatic şi topoclimatic în Subcarpaţii Ialomiţei. Universitatea din Oradea

Baum RL, Fleming RW (1991) Use of longitudinal strain in identifying driving and resisting elements of landslides. Geol Soc Am Bull 103:1121–1132

Benoit L, Briole P, Martin O, Thom C, Malet J-P, Ulrich P (2015) Monitoring landslide displacements with the Geocube wireless network of low-cost GPS. Eng Geol 195:111–121. https://doi.org/10.1016/j.enggeo.2015.05.020

Bolles RC, Baker HH, Marimont DH (1987) Epipolar-plane image analysis: an approach to determining structure from motion. Int J Comput vis 1:7–55. https://doi.org/10.1007/BF00128525

Booth AM, McCarley J, Hinkle J, Shaw S, Ampuero JP, Lamb MP (2018) Transient reactivation of a deep-seated landslide by undrained loading captured with repeat airborne and terrestrial Lidar. Geophys Res Lett 45:4841–4850. https://doi.org/10.1029/2018GL077812

Booth AM, McCarley JC, Nelson J (2020) Multi-year, three-dimensional landslide surface deformation from repeat lidar and response to precipitation: Mill Gulch earthflow, California. Landslides 17:1283–1296. https://doi.org/10.1007/s10346-020-01364-z

Brasington J, Rumsby BT, McVey RA (2000) Monitoring and modelling morphological change in a braided gravel-bed river using high resolution GPS-based survey. Earth Surf Process Landforms 25:973–990. https://doi.org/10.1002/1096-9837(200008)25:9<973::AID-ESP111>3.0.CO;2-Y

Carey JA, Pinter N, Pickering AJ, Prentice CS, Delong SB (2019) Analysis of landslide kinematics using multi-temporal unmanned aerial vehicle imagery, La Honda. California Environ Eng Geosci 25:301–317. https://doi.org/10.2113/EEG-2228

Carnec C, Massonnet D, King C (1996) Two examples of the use of SAR interferometry on displacement fields of small spatial extent. Geophys Res Lett 23:3579–3582. https://doi.org/10.1029/96GL03042

Cheng Z, Gong W, Tang H, Juang CH, Deng Q, Chen J, Ye X (2021) UAV photogrammetry-based remote sensing and preliminary assessment of the behavior of a landslide in Guizhou. China Eng Geol 289:106172. https://doi.org/10.1016/J.ENGGEO.2021.106172

Chitu Z, Bogaard T, Busuioc A, Burcea S, Sandric I, Adler M-J (2017) Identifying hydrological pre-conditions and rainfall triggers of slope failures at catchment scale for 2014 storm events in the Ialomita Subcarpathians, Romania. Landslides 1–16

Conforti M, Mercuri M, Borrelli L (2021) Morphological changes detection of a large earthflow using archived images, LiDAR-derived DTM, and UAV-based remote sensing. Remote Sens. https://doi.org/10.3390/rs13010120

Delacourt C, Allemand P, Berthier E, Raucoules D, Casson B, Grandjean P, Pambrun C, Varel E (2007) Remote-sensing techniques for analysing landslide kinematics: a review. Bull La Société Géologique Fr 178:89–100

Devoto S, Macovaz V, Mantovani M, Soldati M, Furlani S (2020) Advantages of using UAV digital photogrammetry in the study of

slow-moving coastal landslides. Remote Sens. https://doi.org/10.3390/rs12213566

Dille A, Kervyn F, Handwerger AL, d'Oreye N, Derauw D, Mugaruka Bibentyo T, Samsonov S, Malet JP, Kervyn M, Dewitte O (2021) When image correlation is needed: unravelling the complex dynamics of a slow-moving landslide in the tropics with dense radar and optical time series. Remote Sens Environ 258:112402. https://doi.org/10.1016/J.RSE.2021.112402

ESRI (n.d.) ArcGIS Drone2Map | Turn your drone into an enterprise GIS productivity tool [WWW Document]. https://www.esri.com/en-us/arcgis/products/arcgis-drone2map/overview. Accessed 23 Oct 2021

ESRI (n.d.) 2D, 3D & 4D GIS Mapping Software | ArcGIS Pro [WWW Document]. https://www.esri.com/en-us/arcgis/products/arcgis-pro/overview. Accessed 23 Oct 2021

Farr TG, Rosen PA, Caro E, Crippen R, Duren R, Hensley S, Kobrick M, Paller M, Rodriguez E, Roth L, Seal D, Shaffer S, Shimada J, Umland J, Werner M, Oskin M, Burbank D, & Alsdorf D (2007) The Shuttle Radar Topography Mission. Reviews of Geophysics 45(2):RG2004. https://doi.org/10.1029/2005RG000183

Fischler MA, Bolles RC (1981) Random sample consensus: a paradigm for model fitting with applications to image analysis and automated cartography. Commun ACM 24:381–395. https://doi.org/10.1145/358669.358692

Fleming RW, Baum RL, Giardino M (1999) Map and description of the active part of the Slumgullion Landslide, Hinsdale County, Colorado

Fleming RW, Johnson AM (1989) Structures associated with strike-slip faults that bound landslide elements. Eng Geol 27:39–114

Fonstad MA, Dietrich JT, Courville BC, Jensen JL, Carbonneau PE (2013) Topographic structure from motion: a new development in photogrammetric measurement. Earth Surf Process Landforms. https://doi.org/10.1002/esp.3366

Fustos I, Remy D, Abarca-Del-Rio R, Muñoz A (2017) Slow movements observed with in situ and remote-sensing techniques in the central zone of Chile. Int J Remote Sens 38:7514–7530. https://doi.org/10.1080/01431161.2017.1317944

Gili JA, Corominas J, Rius J (2000) Using Global Positioning System techniques in landslide monitoring. Eng Geol 55:167–192. https://doi.org/10.1016/S0013-7952(99)00127-1

Giordan D, Hayakawa Y, Nex F, Remondino F, Tarolli P (2018) Review article: the use of remotely piloted aircraft systems (RPASs) for natural hazards monitoring and management. Nat Hazards Earth Syst Sci 18:1079–1096. https://doi.org/10.5194/nhess-18-1079-2018

Giordan D, Manconi A, Facello A, Baldo M, dell'Anese F, Allasia P, Dutto F (2015) Brief communication: the use of an unmanned aerial vehicle in a rockfall emergency scenario. Nat Hazards Earth Syst Sci 15:163–169. https://doi.org/10.5194/nhess-15-163-2015

Gomez C, Purdie H (2016) UAV- based photogrammetry and geocomputing for hazards and disaster risk monitoring - a review. Geoenvironmental Disasters. https://doi.org/10.1186/s40677-016-0060-y

Guzzi R, Parise M (1992) Surface features and kinematics of the Slumgullion landslide, near Lake City, Colorado. USGS Open-file Rep 92–252

Huang F, Ye Z, Jiang SH, Huang J, Chang Z, Chen J (2021) Uncertainty study of landslide susceptibility prediction considering the different attribute interval numbers of environmental factors and different data-based models. CATENA 202:105250. https://doi.org/10.1016/J.CATENA.2021.105250

Ilinca V, Şandric I, Jurchescu M, Chiţu Z (2021) Identifying the role of structural and lithological control of landslides using TOBIA and weight of evidence: case studies from Romania. Landslides. https://doi.org/10.1007/s10346-021-01749-8

James MR, Robson S, d'Oleire-Oltmanns S, Niethammer U (2017) Optimising UAV topographic surveys processed with structure-from-motion: ground control quality, quantity and bundle adjustment. Geomorphology. https://doi.org/10.1016/j.geomorph.2016.11.021

Kucharczyk M, Hugenholtz CH (2021) Remote sensing of natural hazard-related disasters with small drones: global trends, biases, and research opportunities. Remote Sens Environ 264:112577. https://doi.org/10.1016/J.RSE.2021.112577

Li Y, Huang J, Jiang S-H, Huang F, Chang Z (2017) A web-based GPS system for displacement monitoring and failure mechanism analysis of reservoir landslide. Sci Rep 7:17171. https://doi.org/10.1038/s41598-017-17507-7

Lindner G, Schraml K, Mansberger R, Hübl J (2016) UAV monitoring and documentation of a large landslide. Appl Geomatics 8:1–11. https://doi.org/10.1007/s12518-015-0165-0

Lowe DG (2004) Distinctive image features from scale-invariant key-points. Int J Comput Vis 2004 602 60:91–110. https://doi.org/10.1023/B:VISI.0000029664.99615.94

Lowe DG (1999) Object recognition from local scale-invariant features. Proc IEEE Int Conf Comput vis 2:1150–1157. https://doi.org/10.1109/ICCV.1999.790410

Lucieer A, Jong SM, d., Turner, D., (2014) Mapping landslide displacements using structure from motion (SfM) and image correlation of multi-temporal UAV photography. Prog Phys Geogr 38:97–116. https://doi.org/10.1177/0309133313515293

Manconi A, Casu F, Ardizzone F, Bonano M, Cardinali M, De Luca C, Gueguen E, Marchesini I, Parise M, Vennari C, Lanari R, Guzzetti F (2014) Brief communication: rapid mapping of landslide events: the 3 December 2013 Montescaglioso landslide. Italy Nat Hazards Earth Syst Sci 14:1835–1841. https://doi.org/10.5194/nhess-14-1835-2014

National Administration of Meteorology D (n.d.) National Administration of Meteorology, data

National Institute of Hydrology and Water Management D (n.d.) No title

Niethammer U, James MR, Rothmund S, Travelletti J, Joswig M (2012) UAV-based remote sensing of the Super-Sauze landslide: evaluation and results. Eng Geol 128:2–11. https://doi.org/10.1016/J.ENGGEO.2011.03.012

Parise M (2003) Observation of surface features on an active landslide, and implications for understanding its history of movement. Nat Hazards Earth Syst Sci 3:569–580. https://doi.org/10.5194/nhess-3-569-2003

Pătruţ I (1955) Geologia şi tectonica regiunii Vălenii de Munte-Cosminele-Buştenari. Anu Institutului Geol Al României 28:5–98

Pellicani R, Argentiero I, Manzari P, Spilotro G, Marzo C, Ermini R, Apollonio C (2019) UAV and airborne LiDAR data for interpreting kinematic evolution of landslide movements: the case study of the Montescaglioso Landslide (Southern Italy). Geosci. https://doi.org/10.3390/geosciences9060248

Peternel T, Kumelj Š, Oštir K, Komac M (2017) Monitoring the Potoška planina landslide (NW Slovenia) using UAV photogrammetry and tachymetric measurements. Landslides 14:395–406. https://doi.org/10.1007/s10346-016-0759-6

PIX4D SA C (n.d.) PIX4Dcapture [WWW Document]. https://www.pix4d.com/product/pix4dcapture. Accessed 23 Oct 2021

Popescu-Voiteşti I (1924) Raport asupra alunecărilor de teren de la Poseşti (16 şi 17 aprilie 1915). Rap. Act. al Institutului Geol. al României în 1915 IX, 50–52

Popescu G (1952) Zona flişului paleogen între Valea Buzăului şi Valea Vărbilăului. Dări Seamă 113–125

Qin C-Z, Bao L-L, Zhu A-X, Wang R-X, Hu X-M (2013) Uncertainty due to DEM error in landslide susceptibility mapping. Int J Geogr Inf Sci 27:1364–1380. https://doi.org/10.1080/13658816.2013.770515

Rossi G, Tanteri L, Tofani V, Vannocci P, Moretti S, Casagli N (2018) Multitemporal UAV surveys for landslide mapping and characterization. Landslides 15:1045–1052. https://doi.org/10.1007/s10346-018-0978-0

Samia J, Temme A, Bregt A, Wallinga J, Guzzetti F, Ardizzone F, Rossi M (2017) Do landslides follow landslides? Insights in path dependency from a multi-temporal landslide inventory. Landslides 14:547–558. https://doi.org/10.1007/s10346-016-0739-x

Sandric I, Ionita C, Chitu Z, Dardala M, Irimia R, Furtuna FT (2019) Using CUDA to accelerate uncertainty propagation modelling for landslide susceptibility assessment. Environ Model Softw 115:176–186. https://doi.org/10.1016/j.envsoft.2019.02.016

Santangelo M, Alvioli M, Baldo M, Cardinali M, Giordan D, Guzzetti F, Marchesini I, Reichenbach P (2019) Brief communication: remotely piloted aircraft systems for rapid emergency response: road exposure to rockfall in Villanova di Accumoli (central Italy). Nat Hazards Earth Syst Sci 19:325–335. https://doi.org/10.5194/nhess-19-325-2019

Schulz W, Coe JA, Ricci PP, Smoczyk GM, Shurtleff BL, Panosky J (2017) Landslide kinematics and their potential controls from hourly to

decadal timescales: insights from integrating ground-based InSAR measurements with structural maps and long-term monitoring data. Geomorphology 285:121–136. https://doi.org/10.1016/j.geomorph.2017.02.011

Schulz WH (2007) Landslide susceptibility revealed by LIDAR imagery and historical records, Seattle, Washington. Eng Geol 89:67–87. https://doi.org/10.1016/j.enggeo.2006.09.019

SPH Engineering (n.d.) Ground Station Software | UgCS PC Mission Planning [WWW Document]. https://www.ugcs.com/. Accessed 23 Oct 2021

Squarzoni C, Delacourt C, Allemand P (2005) Differential single-frequency GPS monitoring of the La Valette landslide (French Alps). Eng Geol 79:215–229. https://doi.org/10.1016/j.enggeo.2005.01.015

Ștefănescu M, Rădan S, Micu M, Mărunțeanu M, Ștefănescu M (1978) Harta geologică a României, scara 1:50000, foaia Slănic (Prahova). Institutul Geologic al României, București

Stumpf A, Malet JP, Kerle N, Niethammer U, Rothmund S (2013) Image-based mapping of surface fissures for the investigation of landslide dynamics. Geomorphology 186:12–27. https://doi.org/10.1016/j.geomorph.2012.12.010

Tarchi D, Casagli N, Fanti R, Leva DD, Luzi G, Pasuto A, Pieraccini M, Silvano S (2003) Landslide monitoring by using ground-based SAR interferometry: an example of application to the Tessina landslide in Italy. Eng Geol 68:15–30. https://doi.org/10.1016/S0013-7952(02)00196-5

Türk T (2018) Determination of mass movements in slow-motion landslides by the Cosi-Corr method. Geomatics. Nat Hazards Risk 9:325–336. https://doi.org/10.1080/19475705.2018.1435564

Ullman S (1983) Computational studies in the interpretation of structure and motion: summary and extension. Massachusetts Inst. Technol. Artif. Intell. Lab. A.I. Memo 706, March 1983 1–25

Ullman S (1979) The interpretation of structure from motion. Proc R Soc London Ser B Biol Sci 203:405–426

Ullman S (1976) The interpretation of structure from motion. Massachusetts Inst. Technol. Artif. Intell. Lab. A.I. Memo 476, Oct. 1976 1–7

USGS (2006) FGDC Digital Cartographic Standard for Geologic Map Symbolization (PostScript Implementation). US Geological Survey

Valkaniotis S, Papathanassiou G, Ganas A (2018) Mapping an earthquake-induced landslide based on UAV imagery; case study of the 2015 Okeanos landslide, Lefkada. Greece Eng Geol 245:141–152. https://doi.org/10.1016/J.ENGGEO.2018.08.010

Van Den Eeckhaut M, Poesen J, Verstraeten G, Vanacker V, Nyssen J, Moeyersons J, van Beek LPH, Vandekerckhove L (2007) Use of LIDAR-derived images for mapping old landslides under forest. Earth Surf Process Landforms 32:754–769. https://doi.org/10.1002/esp.1417

Vîrghileanu MR (2018) Subcarpații dintre Prahova și Teleajen. Editura Universității din București, București, Relief-așezări-organizarea spațiului

Westoby MJ, Brasington J, Glasser NF, Hambrey MJ, Reynolds JM (2012) Structure-from-motion photogrammetry: a low-cost, effective tool for geoscience applications. Geomorphology 179:300–314

Wheaton JM (2008) Uncertainty in morphological sediment budgeting of rivers. Unpublished PhD thesis. University of Southampton, Southampton

Wheaton JM, Brasington J, Darby SE, Sear DA (2010) Accounting for uncertainty in DEMs from repeat topographic surveys: improved sediment budgets. Earth Surf Process Landforms 35:136–156. https://doi.org/10.1002/ESP.1886

Williams RD (2012) Section 2.3.2. DEMs of difference. In: Cook SJ, Clarke LE, Nield JM (Eds) Geomorphological techniques (online edition). ISSN: 2047–0371. British Society for Geomorphology, London, pp 1–17

Wilson JP, Gallant JC (2000) Terrain analysis: Principles and applications. Earth Sciences: Geography. Wiley, New York

Yang D, Qiu H, Hu S, Pei Y, Wang X, Du C, Long Y, Cao M (2021) Influence of successive landslides on topographic changes revealed by multitemporal high-resolution UAS-based DEM. CATENA 202:105229. https://doi.org/10.1016/J.CATENA.2021.105229

Zárate BA, Hamdouni RE, Fernández T (2021) GNSS and RPAS integration techniques for studying landslide dynamics: application to the areas of Victoria and Colinas Lojanas, (Loja, Ecuador). Remote Sens 13:3496. https://doi.org/10.3390/RS13173496

Viorel Ilinca · Ion Gheuca

Geological Institute of Romania, Caransebeş Street, no. 1, Bucharest, Romania
Email: ilincaviorel@yahoo.com

Ionuț Șandric (✉) · Radu Irimia

Faculty of Geography, University of Bucharest, Nicolae Bălcescu, no. 1, Bucharest, Romania
Email: ionut.sandric@geo.unibuc.ro

Zenaida Chiţu

National Meteorological Administration, 013686 Bucharest, Romania

Zenaida Chiţu

National Institute of Hydrology and Water Management, 013686 Bucharest, Romania
Email: zenaidachitu@yahoo.com

Viorel Ilinca · Ionuț Șandric · Zenaida Chiţu · Radu Irimia

Institute for Research (ICUB), University of Bucharest, Bucharest, Romania
Email: radu.irimia@geo.unibuc.ro